DEVELOPMENT OF A PROPULSION TEST STAND FOR EVTOL APPLICATIONS

Jan-Arun Faust* Florian M. Heckmeier Marco Stuhlpfarrer
eRC-System GmbH, Einsteinstr. 32, 85521 Ottobrunn, Germany
*Corresponding Author

Abstract

This paper presents the design and implementation of a propulsion test stand developed for testing electric vertical take-off and landing aircraft propulsion systems in hovering operating conditions. The test stand enables a comprehensive evaluation of propulsion systems up to 200 kW, including propellers, electric motors, and electronic speed controllers. The facility features a dedicated real-time high-fidelity data-acquisition system to measure the forces, moments, and vibrations generated by the complete propulsion system. Additional instrumentation setups enable the quantification of the static blade deflection and the propeller acoustics. The test facility incorporates a modular design construction that does not rely on permanent infrastructure and enables the continued development of the propulsion system and corresponding instrumentation.

1. INTRODUCTION

The ongoing development efforts in aviation electrification over the past decade, particularly within the context of urban air mobility, have enabled significant technological advances and the emergence of novel electric vertical take-off and landing (eVTOL) concepts. A common feature of these aircraft is the use of multiple electric propulsion units powering propellers, rotors, and/or fans to provide lift and thrust. Their design and operating scope are specific to the aircraft configuration. With limited data available to describe the custom propulsion systems, full-scale testing capabilities and experimental data are considered essential, and cannot be replaced by simulations alone.

Developing full-scale testing facilities is standard practice across the industry and research institutions. Test rigs such as NASA's Airvolt (Ref. 1) have demonstrated the need of collecting high-fidelity data of propulsion systems to be used in future aircraft (including motor, inverter, and battery), to improve the understanding of the system performance, efficiencies, and thermal dynamics. Furthermore, Bain et al. (Ref. 2) highlight the importance of full-scale testing in capturing the propeller acoustics accurately, with the high importance of broadband noise levels associated with boundary layer transition. Mobile test facilities have also been developed to study full-scale systems in representative flight conditions, without the dependence on wind-tunnels (Ref. 3).

In this context, a full-scale electric propulsion test rig was developed to meet the experimental testing requirements that arise during the development process of eVTOL aircraft at eRC-System. The propulsion test stand (PTS) was built to accelerate system maturity of the custom-developed propellers and corresponding electric propulsion systems in hovering operating conditions. This includes acquiring the necessary data to evaluate and analyze the propeller thrust, power, vibrations, and acoustics. Furthermore, evaluating the propulsion system functionality, dynamics, performance, efficiencies, and thermal rejection are also of great relevance.

The complete test facility, featuring the test rig and surrounding infrastructure, is designed to be operated outdoors and is completely self-contained. A modular design approach to the different components and systems is utilized to facilitate the exchange of hardware components and measurement instrumentation. This also applies to the facility itself; as the various parts do not rely on permanent implementations and can be unmounted, stored, and relocated if required. This paper describes the implemented facility solution and capabilities, alongside the main design considerations that arose during the project.

2. EXPERIMENTAL SETUP DESCRIPTION

The main requirements of the test rig were to accommodate electric propulsion systems on the order of 200 kW and propellers with diameters of up to 2.5 meters. The test rig must also provide accurate measurements for operating conditions that are representative of a propeller in hover. One of the key design drivers was defining the propeller orientation. A vertically aligned propeller axis would closely resemble the installation in the aircraft use case, however, sufficient ground clearance would be required to avoid the ground effect. Reference 4 also demonstrates the need to avoid interference ground effects with any work platforms or safety enclosures that may be required with such a configuration. Meanwhile, a horizontally aligned propeller axis can be subjected to a different kind of interference effect, where the stream tube contraction upstream of the propeller is influenced by the ground, leading to an asymmetric flow field experienced at the propeller plane.

Initial designs suggested that a horizontal propeller axis on a tripod would result in a simpler, smaller, more manageable, and less expensive overall facility solution when accounting for propeller fragment containment, ground effect, and rotor outwash. To estimate the asymmetric interference effect related to the ground on the expected propeller performance, computational fluid dynamic (CFD) simulations were performed. The results suggested that a ground clearance of two propeller radii from the rotational axis would result in minor interference effects. This is comparable with hover performance tests of isolated proprotors conducted at NASA's Outdoor Aerodynamic Research Facility (OARF) test stand (Ref. 5), which according to Harris (Ref. 6) is considered by many to be the "gold standard of hover performance data".

The detailed design and integration process were inspired by the recommendations and best practice guidelines outlined in the development of NASA's Airvolt test bench (Ref. 1). The complete facility is divided into sub-systems, which can be developed, set up, and tested in parallel, before proceeding with the integration of the individual modules. The test rig is seen as a prototyping platform that enables continuous modifications and the integration of different propulsion system components. In the following sections, the fundamental aspects of the baseline configuration, as depicted in Figure 1, are further described.

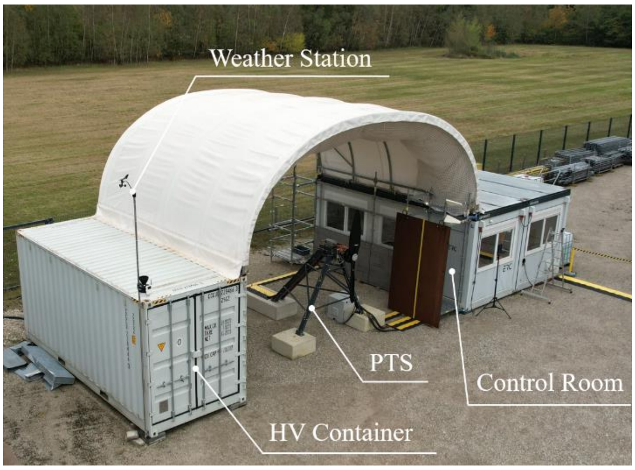

Figure 1: The PTS test facility with its surroundings.

2.1. Infrastructure and Operation

Throughout this project, a holistic safety concept was implemented to reduce potential risks and ensure system safety. These considerations are fundamental to the entire facility infrastructure, which consists of two container units, one serving as a control room, and the other for storing the high-voltage (HV) power supply components. The test area is enclosed between the two container units and a roof structure. A total of three engineers are required to operate the test facility, including a data-acquisition engineer, a propulsion system engineer, and a lead test engineer.

The main consideration behind the implemented solution was to separate operating personnel from potential hazards. All HV-related components are galvanically isolated from the control room and are located on the test rig or stored separately in a climate-controlled HV container. HV state indication lights are installed to signal when HV is enabled. A dedicated emergency shut-off button is installed in the control room to terminate the electrical power output. The propeller rotating plane is offset towards the front of both containers to avoid the direct impact risk of a potential rotor burst. Additionally, steel and polycarbonate plates are mounted to protect the control room from indirect propeller fragments. A real-time camera system is utilized to provide a clear overview of the facility and to record all activities for traceability.

2.2. Test Rig Structure

Figure 2 shows a close-up of the PTS structure. The simple steel tripod structure is divided into three main assemblies: an internal assembly, an upper frame, and the supports and struts. The internal assembly provides the mounting for the electric motor, rotary encoders, and the load cell to the main upper frame. The upper frame contains an additional mounting plate for the electronic speed controllers (ESCs). The ESCs are stacked on top of each other and are positioned directly downstream of the motor to reduce the length of the shielded alternating current (AC) cables and lessen electromagnetic interference (EMI) on the measured data. The supports were fabricated from I-beam elements to reduce the frontal cross-section for less aerodynamic blockage effects. Additional struts connecting the main supports were used to increase the structure stiffness. Multiple design iterations were analyzed using finite element method (FEM) to simulate the expected eigenfrequencies of the main structure. The cross-sections and mounting points were chosen to ensure that no resonance of the excitation frequencies is expected during nominal and peak operating conditions. The test rig is bolted to three separate concrete blocks, which serve as a foundation and counter mass.

Figure 2: Close up of the PTS.

2.3. High Voltage Powertrain Setup

The PTS is designed to remain modular and facilitate the integration of different HV components. A schematic overview of the baseline configuration architecture and components is illustrated in Figure 3. The individual components are summarized in Table 1. The baseline configuration features two custom-built bi-directional AC/DC power supply units (PSUs). These are connected to an electrical control cabinet stored inside the HV container.

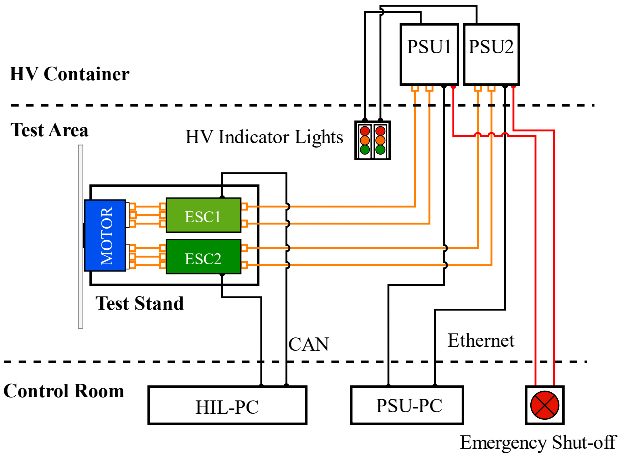

Figure 3: Schematic overview of propulsion system.

Table 1: Baseline PTS configuration

Components	Description	Configuration
1x Electric motor	EMRAX 348	Medium voltage
2x ESCs	Cascadia Motion CM200	DZ, 800VDC
2x Power supplies	iTech ITS 5300	0-1500VDC 90 kW each

Programmable PSUs were preferred over battery systems due to their inherently reduced complexity in operation and added flexibility. PSUs are configurable up to 1500 VDC with a combined peak power output of 180 kW. These can be used to emulate different battery systems and levels of charge. Additional advantages include reduced operation time (without the need to charge) and avoiding fire hazards associated with batteries. Their main downside is the reliance on sufficient power access from the main grid infrastructure.

The test article, in this context, refers to the electrical propulsion system (excluding the power source) and the custom-built eVTOL propeller. The propulsion system features a dual ESC architecture. The two

Cascadia Motion CM200 ESCs are connected to a single axial flux EMRAX 348 electric motor**.** The electric motor is a dual winding motor i.e., a 2x3 phase motor. Each set of three-phase windings is powered by one ESC. The system capabilities and limitations of the baseline configuration are summarized in Table 2. If required, the test article can be extended to include a battery system. Tests have been conducted with a prototype HV battery system (rated at 800V) and operated up to 200 kW.

Table 2: Baseline PTS system capabilities.

Parameter	Limit
Max RPM	4000 RPM
Max power (electrical)	180 kW
Continuous power (electrical)	180 kW
Max torque	1000 Nm
Continuous torque	500 Nm

The ESCs and electric motor are water-cooled, with each component featuring a separate cooling pump and reservoir. This setup can manipulate and monitor the cooling capacity of each component independently. Thus, it is possible to derive the cooling requirements and evaluate their respective performance under nominal and degraded conditions.

The ESCs use resolvers as sensors to measure the speed and position of the rotor for controlling the motor**.** Both ESCs control the electric motor by using a torque control method which works based on the field-oriented control (FOC). A “Hardware in the Loop” (HIL) PC is used as a control computer to provide the commands and to monitor the feedback from the ESCs. A CAN communication protocol is used to communicate between the HIL-PC and the ESCs. HIL-GUI panels are used to visualize real-time data, issue commands, and broadcast messages to both ESCs. The propulsion engineer intervenes based on the panel feedback when a fault occurs, or parameters reach a specified threshold. The ESCs broadcast various parameters that indicate their status, including voltage, current, torque, temperature, operational state, and any faults. This information is recorded via the HIL-PC and is used to analyze the performance of the ESCs during tests. When the HV battery is used as a power source, its monitoring and control are also managed by the HIL-PC. A separate PC is used to control the PSUs by running the provided battery emulation software and logging the DC voltage and current measurements.

2.4. Data-Acquisition System

As indicated above, the main intention of the PTS is to test and get a better understanding of the complete propulsion system. This concerns both the operational aspects of the propulsion system and the assessment of performance and limitations across different operating conditions. Simple performance metrics can be used to evaluate the electric propulsion system efficiency $\eta_{electrical}$, including the losses associated with the electric motor, ESCs, and wiring:

$$\eta_{electrical} = \eta_{motor} \cdot \eta_{ESC} \cdot \eta_{wiring}$$

$$\eta_{electrical} = \frac{P_{mechanical}}{P_{electrical}} = \frac{torque \cdot rotor\ speed}{voltage \cdot current}$$

Similarly, the figure of merit (FM) can be evaluated to determine the propeller hovering efficiency:

$$FM = \frac{P_{induced}}{P_{mechanical}}$$

$$with\ P_{induced} = \sqrt{\frac{thrust^3}{2 \cdot density \cdot area}}$$

Both efficiency metrics require additional sensors to measure the rotor torque, rotational speed, ambient air density, and thrust. High importance was also placed on measuring the complete forces, moments, and vibrations generated by the entire propulsion system. Consequently, a dedicated data-acquisition (DAQ) system was configured and implemented to collect reliable and accurate data with a high temporal resolution. The system transmits data to separate panels in real time, allowing the data-acquisition engineer to monitor operations and intervene if the measurements exceed safety critical values. The next subsections give a more detailed summary of the utilized data-acquisition hardware.

2.4.1. General Measurement Setup

Figure 4 shows a side view of the PTS with the installed sensors, while Figure 5 provides a schematic overview of the DAQ system. For the transient data acquisition, a NI cDAQ-9189 chassis with separate measurement modules is used. To accommodate potential future upgrades, the ethernet-based NI chassis was chosen, which can be easily connected and synchronized using daisy chaining. All modules are synchronized with an internal clock and by a common measurement task in LabVIEW. All sensor data are stored as additional metadata (sensor specs and calibration data) within the .tdms data files.

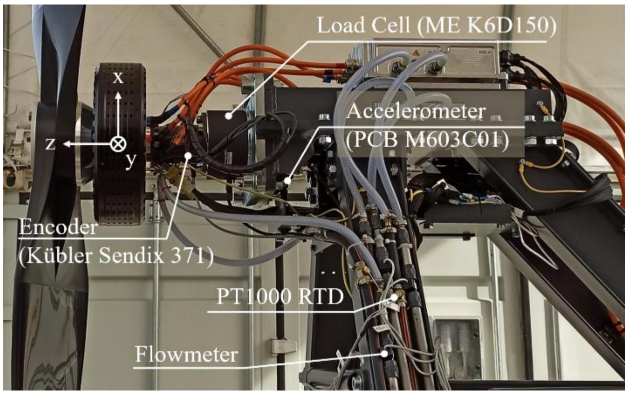

Figure 4: Side view of the PTS with applied sensors.

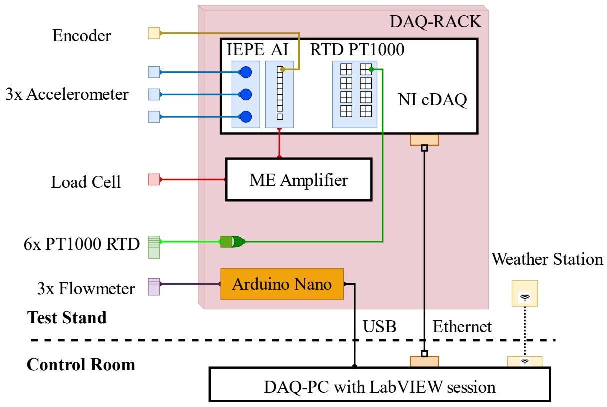

Figure 5: Data-acquisition system schematic.

The main instrumentation effort focuses on the accuracy and temporal resolution of the load cell measurements. The six-component ME K6D150 load cell is connected to the ME GSV-8 amplifier. By applying both a linear and an additional non-linear calibration matrix, unwanted coupling effects to the accuracy of the measured forces and moments, e.g., due to temperature influences, are thus considered, mitigated, and lead to an accuracy class of 0.2. The forces and moments are calculated in engineering units and are transmitted as an analog output from the ME amplifier to the NI-9201 analog input module. The resulting ranges and resolution of the corresponding forces and moments are summarized in Table 3.

Table 3: ME K6D150 load cell specification.

Force/Moment	Rated	Resolution
F_x [N]	10000	0.5
F_y [N]	10000	0.5
F_z [N] (thrust)	25000	1.25
M_x [Nm]	1000	0.05
M_y [Nm]	1000	0.05
M_z [Nm] (torque)	1000	0.05

To investigate the vibration levels, three uniaxial PCB M603C01 IEPE accelerometers are mounted on the PTS upper frame, directed at separate axes, and wired to the NI-9230 IEPE module. The sensors provide a measurement range of 50 g.

The ME amplifier acquires and processes the load cell data with a sampling frequency of $f_{S,ME}$=2400 Hz. All data processed with the NI chassis are sampled at a higher sampling frequency of $f_{S,NI}$=12800 Hz. To account for aliasing problems, a low-pass filter below the Nyquist-Shannon frequency $f_{LP} \leq f_{S,NI}/2$ is applied in the NI modules. To reduce EMI disturbances in the measured data, the cable lengths for the analog sensors are kept to a minimum by placing the NI chassis and ME amplifier in a separate electromagnetically grounded housing next to the main structure.

A separate Kübler Sendix 3671 encoder is installed on the motor drive shaft to measure rotor position and speed within the DAQ system. The analog sensor output is connected to the analog IO module. The resolution of the encoder and the measuring card enables an azimuthal resolution of approximately 2° at the peak-rated RPM.

To monitor the heat rejection of the electric motor and ESCs, a pair of PT1000 RTD sensors are installed at the coolant inlet and outlet ports of each circuit. The analog signal is connected to an RTD NI-9226 module and updated with 1 sample/s. Additionally, a flow rate sensor is integrated into the circuit, and the flow rate data is processed by an Arduino Nano microcontroller. Lastly, environmental data such as pressure, temperature, humidity, wind, and wind direction are measured with a wireless Davis Vantage Pro 2 weather station and recorded in the data files.

2.4.2. Acoustic Measurement Setup

In addition to the previously described DAQ system, a second instrumentation setup for aeroacoustics measurements can be installed and operated independently (see Figure 6). Using 1/2" IEPE free-field microphones (a combination of PCB 377B02 microphone and PCB 426E01 preamplifier) and the Dewesoft SIRIUS mini data collection system, a setup of up to four synchronized microphones can be realized. The dynamic range (3% distortion limit) lies at 137 dB re 20 μPa with a frequency range (+-2 dB) from 3.75 to 20000 Hz. The sound recordings are then acquired and stored in the DewesoftX software.

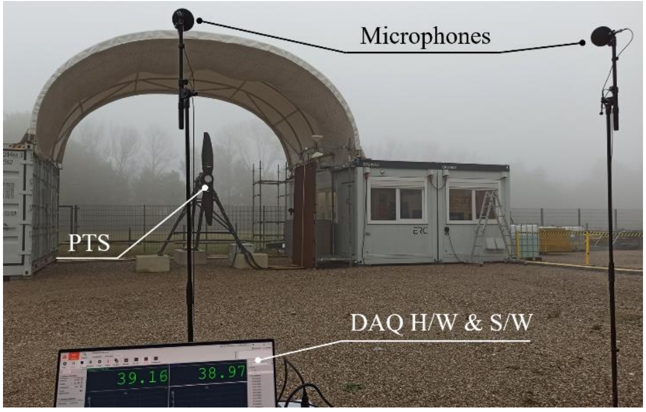

Figure 6: Acoustics measurement setup for the PTS.

All acoustic-related measurements are conducted at low-wind-speed conditions. During these tests, microphones are positioned at a fixed distance from the propeller origin and at different angles relative to the propeller axis. It is important to note that the test stand and surrounding infrastructure are not acoustically treated. The additional interactions, motor noise, and reflections are expected to contribute to the measured acoustics. As suggested by Reference 2, it is assumed that these experimental effects are likely to be similar between different propellers, which allows for a relative comparison between designs. Johnson et al. (Ref. 7) were able to demonstrate that the reflections of nearby buildings would only marginally increase the measured sound pressure level of a similar rotor test stand. For this application, however, due to the proximity of the container and roof structure to the test rig, their reflections and contributions are expected to be more significant. To improve the data correlation with simulated values, the acoustic data is further processed to separate the broadband noise and the tonal noise contributions.

3. Data Post-Processing and Evaluation

The data post-processing and evaluation are crucial in understanding and leveraging the collected experimental data. The primary purpose of the measured data is to enhance the system level understanding and enable a quantitative evaluation of the tested propulsion system in static-thrust conditions. A series of tests is performed throughout the test campaign with various objectives in mind.

The tests vary from long-duration testing, such as monitoring the thermal system behavior, to quick dynamic steps for evaluating transient characteristics, identifying system parameters, and tuning the system responses. Additionally, the tests include assessing the system performance and functionality in nominal and degraded conditions. Each set of tests requires different post-processing methods and analyses.

After each test, all the separate datasets are combined and stored. The data from the propulsion and data-acquisition system are synchronized in post-processing, based on a common time base. In the following, various post-processing steps are shown which should serve as examples to show the versatility of the test stand application.

3.1. Data Phase-Averaging

Data phase-averaging is essential in studying the underlying system behavior related to forces, moments, and vibrations. The DAQ system was configured to accurately capture the high-frequency excitations occurring over a single propeller revolution. The phase averaging process is also employed for uncertainty analysis of the acquired data. The precision uncertainties in the measured forces, moments, and vibrations are determined by calculating the standard deviation of the mean measurement value at each azimuth location. The average of the entire revolution is then taken to obtain the reported data point uncertainty.

The post-processing routine is outlined in Figure 7. As a first step, the raw data is visualized and judged based on their general time domain representation. Data statistics already indicate corrupted measurements or outliers. Eliminating these outliers allows for a more accurate characterization of the propeller. A dedicated “time frame” identification routine extracts measured segments with equivalent RPM readings within a predefined fluctuation range for further analysis. By mapping the measured values to the corresponding blade position, these bundled time frames are processed to give a 360°-azimuthal representation of the measured quantities in the time domain, see Figure 8. In this exemplary data, phase-averaged forces, moments, and accelerations are depicted for one test point.

The F_x, F_y, and F_z forces, along with the M_y moment, exhibit a distinct two-per-revolution signal pattern, which corresponds to the propeller blade count and can be attributed to propeller aerodynamic effects and structure dynamics. Additionally, a ten-per-revolution torque ripple (M_z) is evident, which is related to cogging torque. This periodic variation in torque is

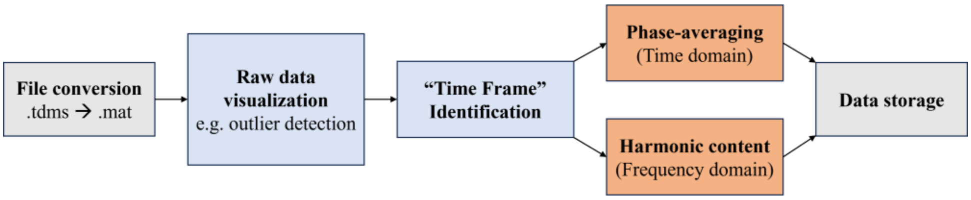

Figure 7: Post-processing routine flow chart.

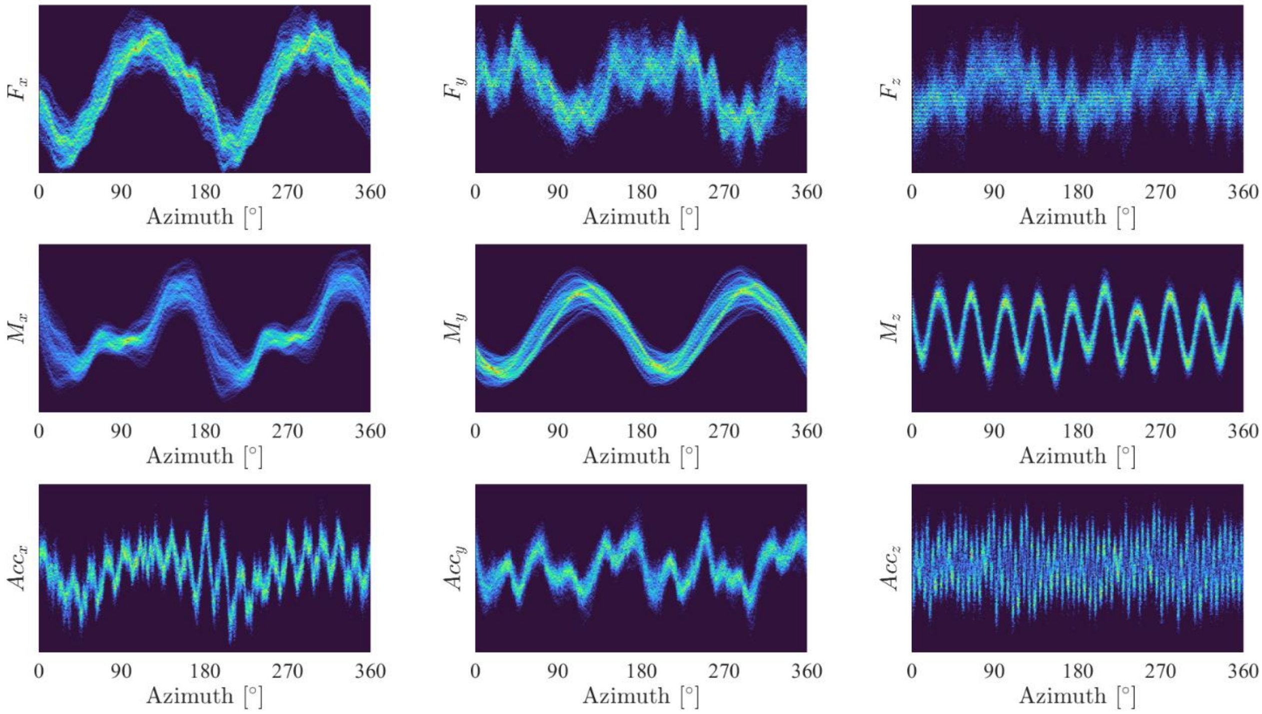

Figure 8: Exemplary phase-averaged data of forces, moments, and accelerations of one test point.

due to the interactions between the rotor's permanent magnets and the stator's magnetic field, leading to changes in reluctance depending on the rotor's position. These high frequency oscillations are also captured in the measured forces (F_x, F_y, F_z), which are characterized by a superstition of the two harmonics.

At higher speeds, the motor moment of inertia suppresses the effects of cogging torque resulting in a different harmonic composition. It is difficult to isolate the effects of the individual sources, as the DAQ system measures the coupled dynamics of the entire system, including the aerodynamics, blade structure dynamics, cogging torque, inertia, and test rig structure dynamics. The harmonic content of the phase-averaged data is investigated within the frequency domain spectra across a range of thrust conditions. The analysis provides insights into which harmonics are dominant and are amplified depending on the test setup configuration and operating condition.

3.2. Performance Evaluation

For each test configuration, the performance of the propeller and propulsion system is measured and evaluated across an operating range. This involves performing measurements for 30 second intervals at predefined constant torque levels. Repeated measurements are conducted to reduce the impact of external influences (e.g., wind). In post-processing, the mean values of each test point are used to evaluate the propeller hovering efficiency and propulsion system electric efficiency (as shown in Figure 9 and Figure 10, respectively). By comparing these across different test configurations, the effect of different structural blade compositions, propulsion cooling conditions, and propulsion operating modes can be judged, for instance.

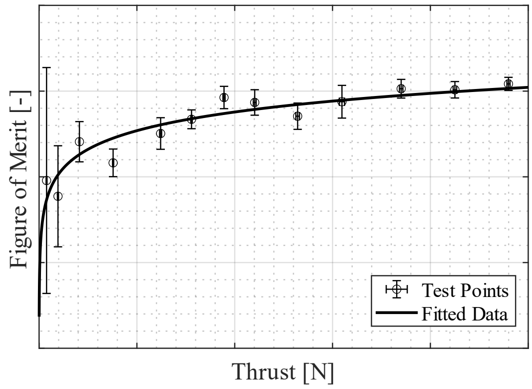

Figure 9: Measured figure of merit in relation to propeller thrust.

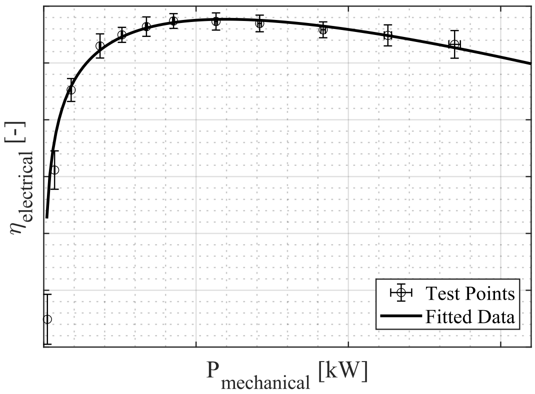

Figure 10: Measured electrical efficiency in relation to mechanical power.

3.3. Vibration Data Post-Processing

The acceleration data are post-processed in both the time and frequency domain for a detailed analysis. By analyzing the vibration content, undesirable effects can be investigated, addressed, and mitigated by e.g. evaluating the influence of dynamic propeller balancing. In the vibration analysis, statistical figures like the peak acceleration, root mean square (RMS) acceleration, crest factor, and standard deviation as well as derived quantities like the RMS velocity and RMS displacement are evaluated. Amplitude spectra and spectrograms give insight into the frequency content of the vibrations. In Figure 11, exemplary power spectral density (PSD) spectra of the three accelerometers are presented. Furthermore, a cumulative view of the composition of the RMS accelerations is shown in Figure 12, providing insights into the main harmonic contributions to the overall vibration levels. By studying these across the operating range, unwanted operating conditions that enhanced vibrations and resonance can be easily detected.

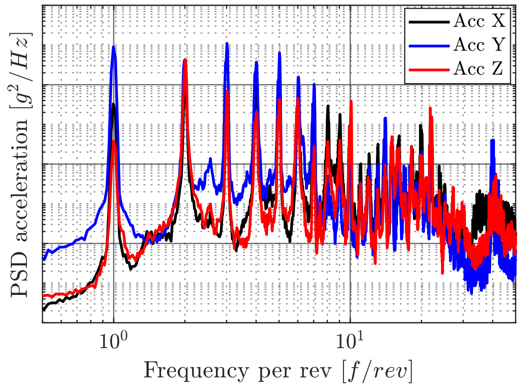

Figure 11: PSD of accelerations over the frequency spectrum.

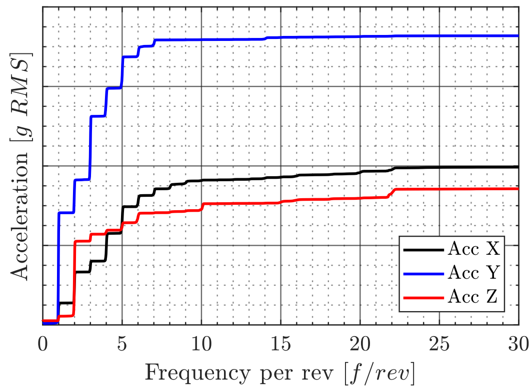

Figure 8: Cumulative composition of RMS acceleration over the frequency spectrum.

3.4. Optical Blade Deflection Analysis

A simple setup can be utilized to roughly quantify the blade tip deflection in thrust direction with acceptable accuracy. For these tests, a GoPro Hero10 Black action camera is aligned with the propeller rotation plane and centered on the blade tip with a high contrast background (as seen in Figure 13). For each separate test point, a video of 30 seconds is taken at 240 frames per second. The video file is post-processed to roughly quantify the blade tip deflection using basic image processing techniques.

Firstly, each frame in the video file is imported and cropped to a smaller section that is relevant to the blade tip section. Secondly, gray scaling is applied, and a detection process is used to identify if a blade is present in the current frame and selected for further processing. Thirdly, Gaussian filters and image flattening are applied before binarizing the image. Next, an overlay of all the relevant images from the video file is generated. Lastly, the blade tip location is compared with that of a stationary blade and scaled to a distance using pixel correlation from calibration images. This basic instrumentation setup provides a quick means to provide insights into blade deflection at different thrust levels, as depicted in Figure 14.

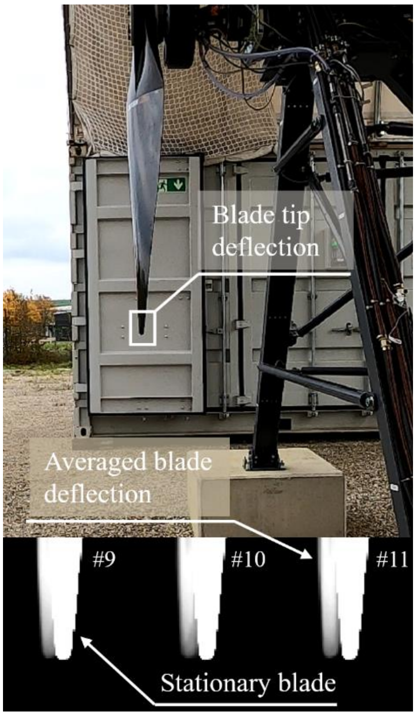

Figure 9: Image-processing steps in blade deflection analysis.

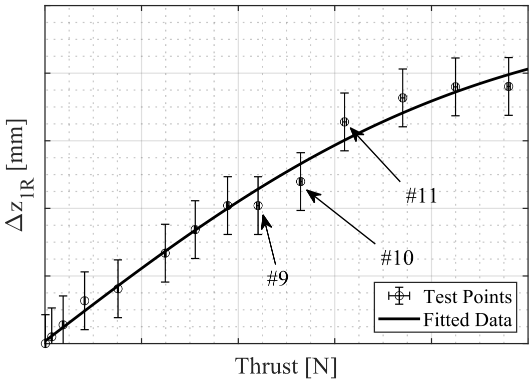

Figure 14: Optical propeller blade deflection measurements using video camera footage.

4. CONCLUDING REMARKS

The availability of high-fidelity full-scale test stands is crucial in improving the understanding of electric propulsion systems. The present work describes the initial configuration of a propulsion test stand developed at eRC-System. The implemented facility demonstrates the feasibility of utilizing temporary elements to set up, operate, and conduct full-scale tests reliably and safely. With the current configuration, high-fidelity data can be acquired to provide insights into the resulting forces, moments, and accelerations generated by the entire propulsion system. Further measurement setup extensions can be utilized to measure the propeller acoustics and roughly quantify the blade deflection under load. The test rig utilizes a modular design approach, enabling the modification and further development to improve the data quality and system functionality. Additional developments are planned, including the integration of a custom speed controller and a fully integrated cooling circuit. The inclusion of additional current and voltage sensors between the motor and ESCs will enable the individual efficiency evaluation of each component. Furthermore, while the current facility was constructed for a specific test location, the dependency on the electrical infrastructure to power the PSUs could impose constraints on where the facility can be operated in the future. With the inclusion of a dedicated battery system, the facility could achieve greater long-term operational flexibility and benefit from additional electrical power scaling potential.

Author contact:

Jan-Arun Faust, faust@erc-system.com

Florian M. Heckmeier, heckmeier@erc-system.com

Marco Stuhlpfarrer, stuhlpfarrer@erc-system.com

5. ACKNOWLEDGMENTS

The authors would like to thank the team members Michael Seemann, Christopher Schropp, Bastian Scheufele, Sascha Voitle, Nihal Vantagodi, Roland Feil, Marco Häde, and Alexander Gürgens for their invaluable contributions towards the design, assembly, integration, and operation of the PTS.

6. REFERENCES

1. Samuel, A., and Lin, Y., “Airvolt Aircraft Electric Propulsion Test Stand,” 51st AIAA/SAE/ASEE Joint Propulsion Conference, Orlando, FL, July 2015.

2. Bain, J., Mikić, G. V., and Stoll, A., S. G., “Aerodynamic and Aeroacoustic Design of the Joby Aviation eVTOL Propeller,” Vertical Flight Society's 77th Annual Forum and Technology Display, Virtual, May 2021.

3. Papathakis, K. V., Kloesel, K. J., Lin, Y., Clark. S., Ediger, J. J., and Ginn, S., „Design and

Development of a 200-kW Turbo-electric Distributed Propulsion Testbed," 52nd AIAA/SAE/ASEE Joint Propulsion Conference, Salt Lake City, UT, July 2016.

4. Helf, S., Broman, E., Gatchel, S., and Charles, B., "Full-Scale Hover Test of a 25-Foot Tilt Rotor," NASA CR 114626, 1973.

5. Felker, G. G., Betzina, M., and Signor, D., "Performance and Loads Data From a Hover Test of a Full-Scale XV-15 Rotor," NASA TM 86833, 1985.

6. Harris, F. D., "Hover Performance of Isolated Proprotors and Propellers – Experimental Data," NASA CR 219486, 2017.

7. Johnson, C., Sirohi, J., Jacobellis, G., and Singh, R., "Experimental and Computational Investigation of Rotor Noise in Hover," *Journal of Aircraft*, Vol. 61, (3), May-June 2024, pp. 1006-1015. DOI: 10.2514/1.C037039.